Supporting Information

Redesigning Solvation Structure toward Passivation-Free Magnesium Metal Batteries

Juncai Long,[a] Yi Liu,[a] Ze He,[a] Shuangshuang Tan,[c] Fangyu Xiong,[c] Hantao Xu,[a] Weixiao Wang,[a] Ge Zhang,[a] Zhongzhuo Yang[a] and Qinyou An[a, b]*

[a]State Key Laboratory of Advanced Technology for Materials Synthesis and Processing, Wuhan University of Technology, Wuhan 430070, P. R. China

[b]Hubei Longzhong Laboratory, Wuhan University of Technology (Xiangyang Demonstration Zone), Xiangyang 441000, P. R. China

[c]College of Materials Science and Engineering, Chongqing University, Chongqing 400044, P. R. China

* Corresponding Author: Prof. Qinyou An, e-mail: anqinyou86@whut.edu.cn

Material synthesis: All reagents were received from Sigma-Aldrich or Aladdin and used without further purification. The CuS[1], δ-MnO_2[2] and FeHCF[3] cathode materials was synthesized according to previous work. The CuS, MnO_2 and FeHCF cathodes were prepared by spreading the mixed slurry composed of 60 wt% cathode powder, 30 wt% super P, and 10 wt% polyvinylidene fluoride (PVDF) in NMP solvent to stainless steel (SS) foils and dried at 70 °C. The mass loading of the active material is about 1.5 mg cm^{-2}.

Materials characterizations: Fourier transform infrared (FTIR) spectra were measured by using Nicolet iS50 FTIR spectrometer in diffuse reflectance mode. ^{1}H and ^{19}F Nuclear Magnetic Resonance (NMR) spectra were collected using a Bruker 600 MHz spectrometer. In order to eliminate the effect of deuterated reagents on the electrolyte test, the NMR test is performed using the internal standard method (with D_2O).[4] Raman spectra were obtained using a Renishaw INVIA micro-Raman spectroscopy system. The crystals of $Mg(HFIP)_2$ electrolyte for single-crystals XRD studies were obtained by slowly evaporating the solvent in clear $Mg(HFIP)_2$ electrolyte. Data collection was collected at 296 K on a Bruker Smart Apex II diffractometer using Mo-Kα radiation (λ = 0.71073 Å). Calculations and refinement of structures were carried out using APEX2, SHELXTL, and Olex2 software. X-ray photoelectron spectroscopy (XPS) measurements were carried out using Kratos Axis Supra XPS instrument. Thermo Scientific Q Exactive Mass Spectrometer was used to quantitatively analyze the electrolyte components. TOF-SIMS measurements were conducted with a ULVAC-PHI PHI nano TOF 3 instrument. JEOL-7100F microscope was utilized to collect scanning electron microscopy (SEM) images and energy dispersive spectrometry (EDS) elemental mappings. Pair distribution function (PDF) tests were performed to investigate the sample structure by using a D8 Advance X-ray

diffractometer with Ag Kα radiation. For the characterization of SEI, Mg||Mg symmetrical cells with different electrolytes were disassembled after 20 charge-discharge cycles at a current density of 0.1 mA cm^{-2}, 1 h charging and 1 h discharging. Then, the cycled Mg metal electrodes sample were rinsed with dry DME (3 times) in glove box.

Electrochemical measurement: CR2016 coin cells were assembled in an Ar-filled glove box with Mg metal foil as the anode, glass fiber membrane (GF/A What-man) as the separator. The electrochemical performance of the batteries was performed by using a multi-channel battery test system (NEWARE Battery Test System, Shenzhen, China, CT-4008-5V 10mA-164 and LAND CT2001A) at room temperature. CE measurements were conducted using asymmetric Mg||Cu cells. The cells were discharged for 30 minutes and charge to 1.5 V at a current density of 0.5 mA cm^{-2}. Besides, the standard Aurbach method has also been used to test the CE.[5] Symmetric Mg||Mg cells were assembled for evaluating the polarization properties of the electrolyte. Cyclic voltammetry (CV) curves and linear scan voltammetry (LSV) were tested using a BioLogic VMP3 multichannel electrochemical workstation. The CV was studied by a three-electrode system using Mg as the reference and counter electrode and SS as the working electrode at a scanning rate of 25 mV s^{-1}. LSV was carried out using Al, Cu, SS, Ti and Mo foils as the working electrode and Mg foil as the reference and counter electrode. The scan rate was 10 mV s^{-1}.

Theoretical Calculation

DFT calculation: All calculations model have been fully optimized on Gaussian 09 package and calculated at B3LYP/6–311G(d,p) and B3LYP/6–311+G(d,p) levels. The parameters of DME solvents are as follows:[6]

stoichiometry=$C_4O_2H_{10}$

solventname=DimethoxyEthane

eps=7.55

epsinf=1.896129

hbondacidity=0.00

hbondbasicity=0.68

SurfaceTensionAtInterface=35.4216652

CarbonAromaticity=0.0

ElectronegativeHalogenicity=0.0

The desolvation process was simulated using Gaussian09 software. During these simulations, the B3LYP/6-311G(d,p) was employed, with particular attention paid to changes in electronic charge throughout the desolvation steps. Given the stronger electrostatic interactions between the Mg^{2+} ion and the $HFIP^-$ and $PFTB^-$ anions compared to its interactions with neutral molecules such as DME, the desolvation process primarily focused on the removal of $HFIP^-$ and $PFTB^-$ from Mg^{2+}. The desolvation was modeled in two distinct steps, with one anion (either $HFIP^-$ or $PFTB^-$) being removed in each step.

Desolvation is a process by which solvent molecules are systematically removed from a solute. A general formula to compute the energy changes across multiple desolvation steps is as follows

$$E_{\text{des}} = \sum_{i=1}^{n} (E_i - E_{i-1})$$

Here, E_i and $E_{i\text{-}1}$ represent the total energy of the system after and before the desolvation step, n is the number of desolvation steps.

Molecular Dynamics Simulation： The partial charge of $Mg(TFSI)_2$，$Mg(HFIP)_2$, $Mg(PFTB)_2$ and DME molecule was calculated using Gaussian 16 code and the 6–311G(d,p) basis functions were applied. The OPLSS-AA force field and MKTOP were used to parametrize all atoms, such as the bond parameters, angle parameters and the dihedral angles, and so on. The coordination structure of Mg^{2+} ions in electrolyte were simulated by molecular dynamics (MD) simulation. In system 1, 50 $Mg(TFSI)_2$ and 481 DME molecule were randomly inserted into a cube box with a side length of 7.0 nm. In system 2, 50 $Mg(HFIP)_2$ and 481 DME molecule were randomly inserted into a cube box with a side length of 7.0 nm. In system 3, 50 $Mg(PFTB)_2$ and 481 DME molecule were randomly inserted into a cube box with a side length of 7.0 nm.

The MD simulations were performed in the GROMACS 2021 software package. The steepest descent method was applied to minimize the initial energy for each system with a force tolerance of 1 kJ/(mol^{-1} nm^{-1}) and a maximum step size of 0.002 ps before MD calculations. In all the three directions, periodic boundary conditions were imposed. Leapfrog algorithm was used to integrate the Newtonian equation of motion. The MD simulation was processed in an NPT ensemble and the simulation time is 20 ns. In NPT simulations, the pressure was maintained at 1 bar by the Berendsen barostat in an isotropic manner was performed for constrain bond lengths of hydrogen atoms. The Particle-Mesh-Ewald (PME) with a fourth-order interpolation was used to evaluate the electrostatic interactions and the grid spacing is 1.0 Å, whereas a cutoff of 1.0 Å was employed to calculate the short-range van der Waals interactions. Besides, we also provide typical MD input files as supplementary information.

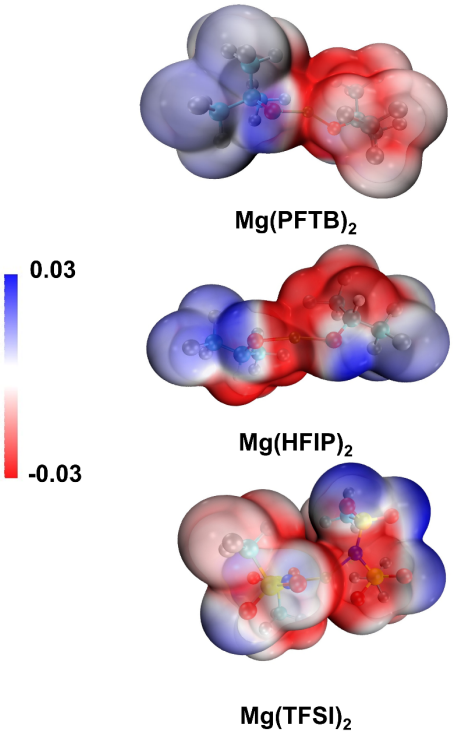

Figure S1. Electrostatic potential (ESP) maps of $Mg(PFTB)_2$, $Mg(HFIP)_2$ and $Mg(TFSI)_2$. Yellow, N; red, O; gray, H; blue, C; orange, Mg.

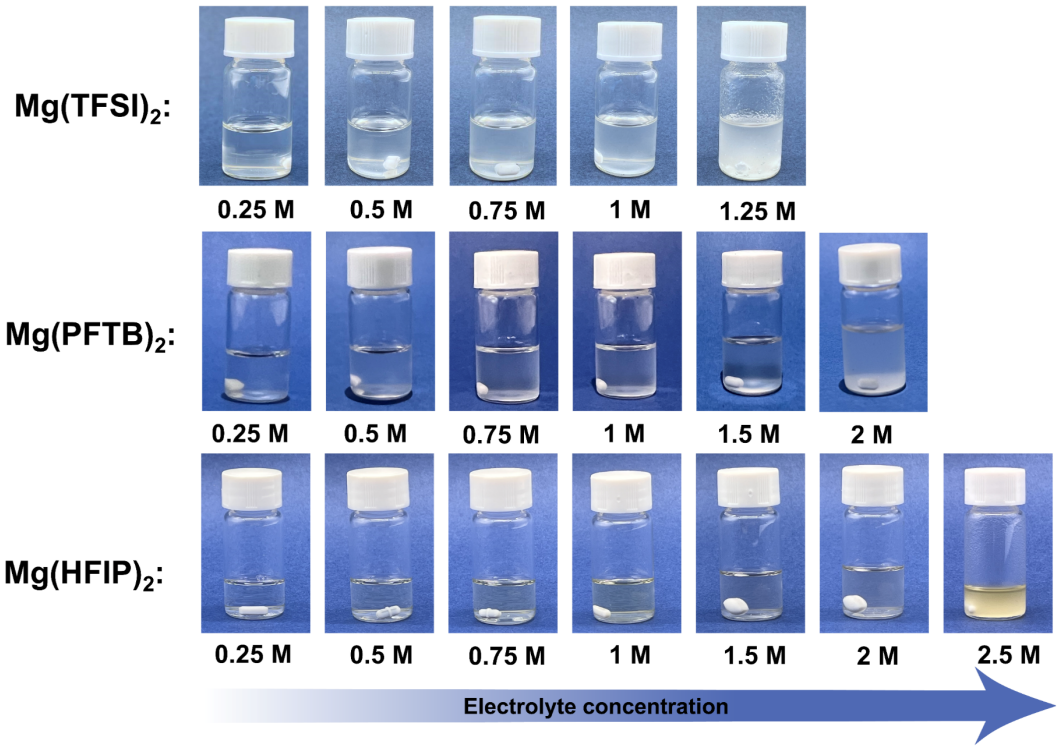

Figure S2. Ultimate solubility test of various simple Mg salts in DME.

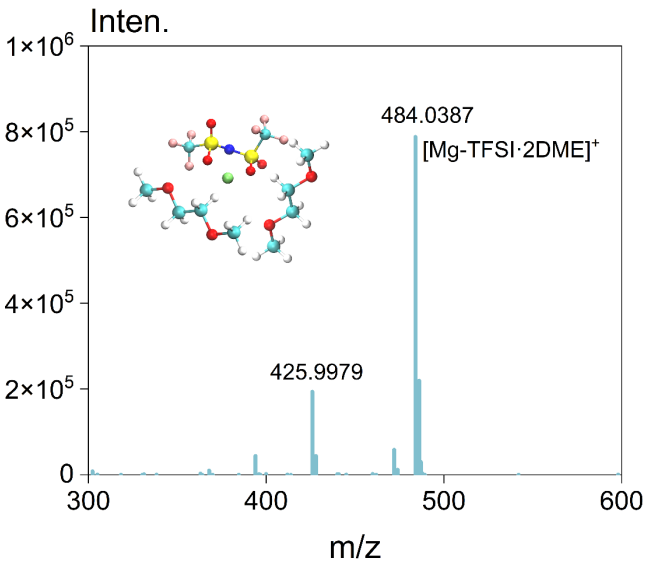

Figure S3. MS results of 0.5 M $Mg(TFSI)_2$/DME electrolyte in positive ion mode.

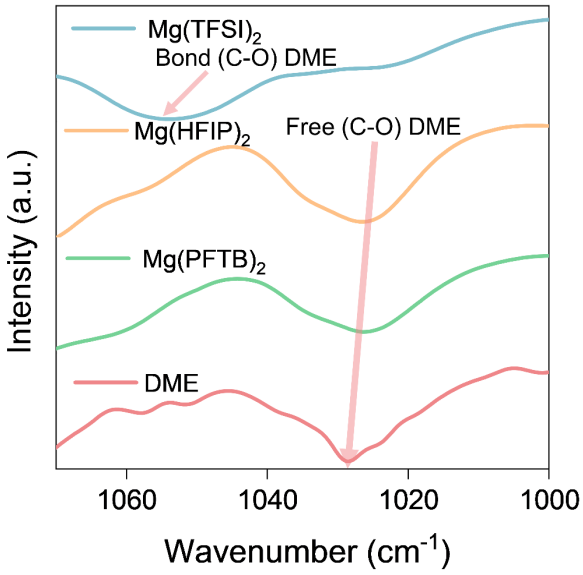

Figure S4. FTIR spectra of pure DME and various electrolytes with 0.5M concentration.

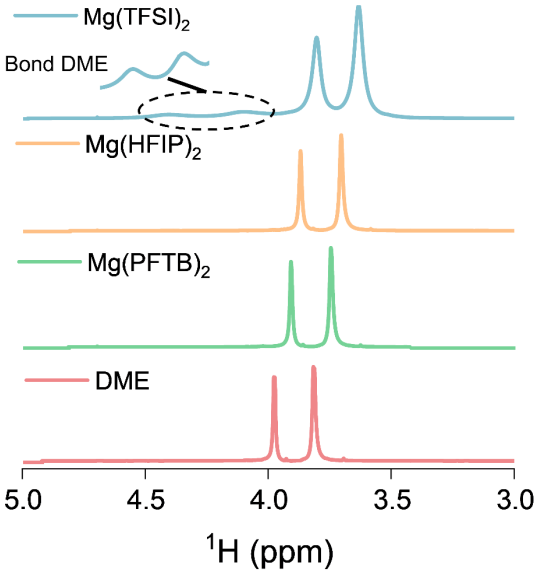

Figure S5. Liquid-state NMR spectra of ^{1}H in various electrolytes with 0.5M concentration, the inset shows an enlarged view of bond DME ($Mg^{2+}(DME)_3$) in $Mg(TFSI)_2$ electrolyte.

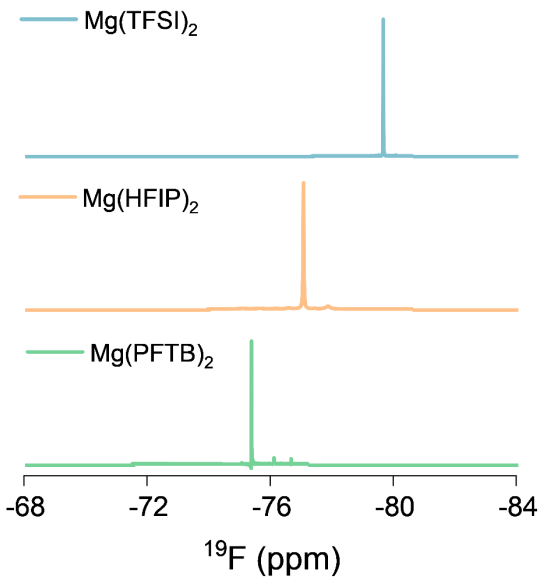

Figure S6. Liquid-state NMR spectra of ^{19}F in different electrolytes with 0.5M concentration.

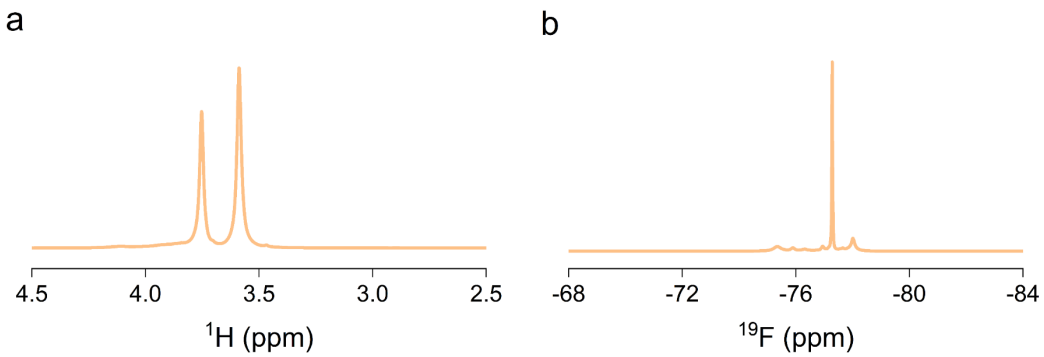

Figure S7. Liquid-state NMR spectra of (a) ^{1}H and (b) ^{19}F in $Mg(HFIP)_2$ electrolyte with 2 M concentration.

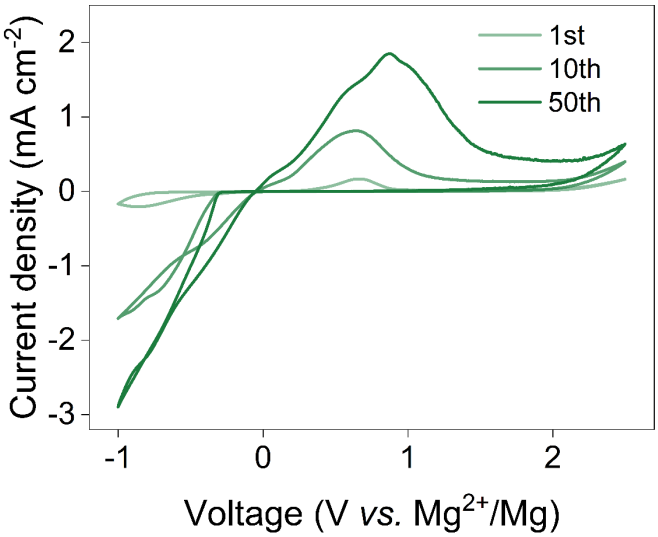

Figure S8. Cyclic voltammograms of the Mg plating/stripping process in 0.5 M $Mg(PFTB)_2$ electrolyte at 25 mV s^{-1}.

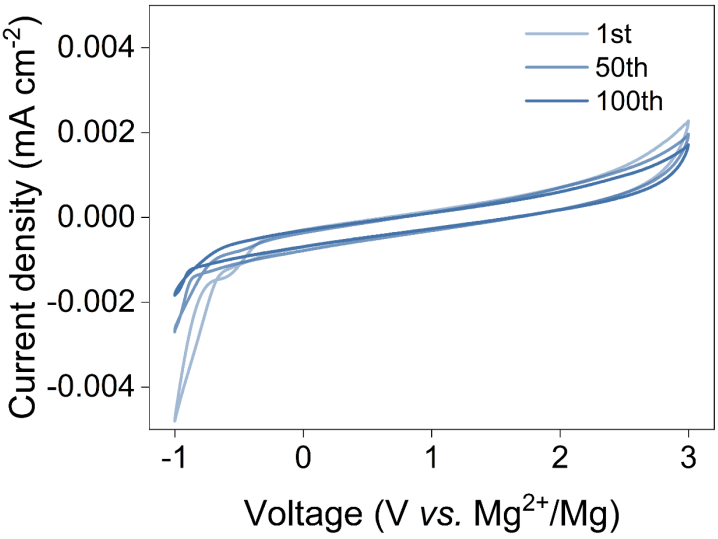

Figure S9. Cyclic voltammograms of the Mg plating/stripping process in 0.5 M $Mg(TFSI)_2$ electrolyte at 25 mV s^{-1}.

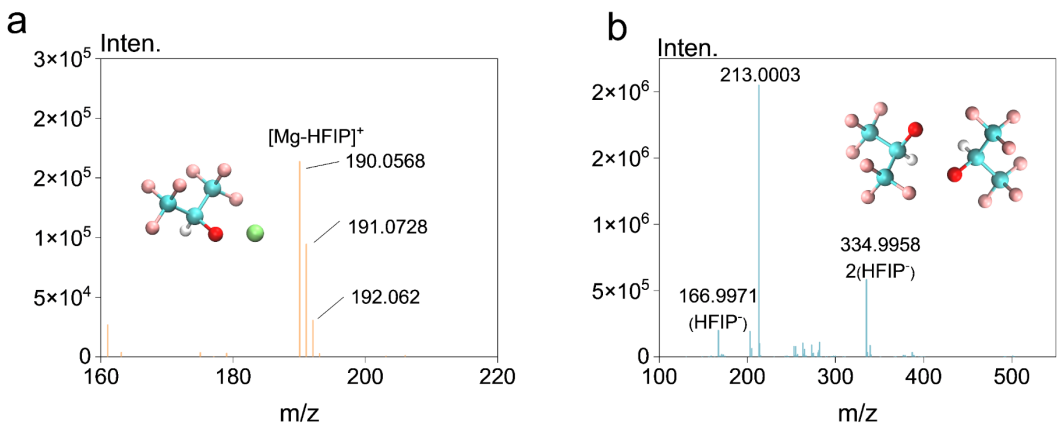

Figure S10. MS results of 2 M $Mg(HFIP)_2$ electrolyte in (a) positive ion mode and (b) negative ion mode.

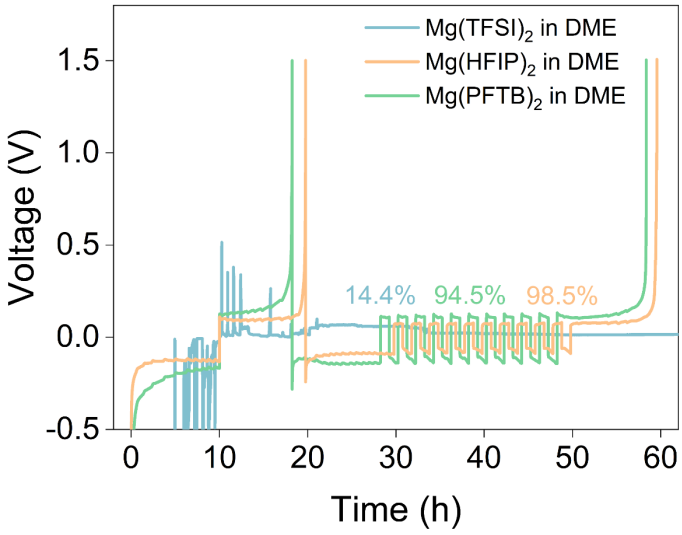

Figure S11. Average CE test of various electrolytes by the standard Aurbach method.

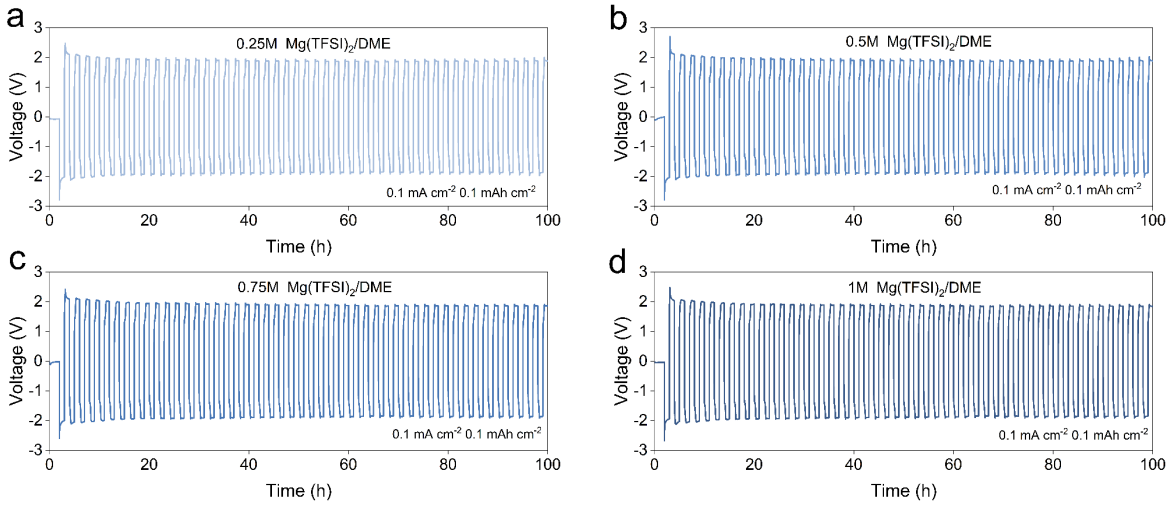

Figure S12. Cycling performance of the Mg||Mg symmetric cells with $Mg(TFSI)_2$ electrolyte in different concertation at 0.1 mA cm^{-2} and 0.1 mAh cm^{-2}.

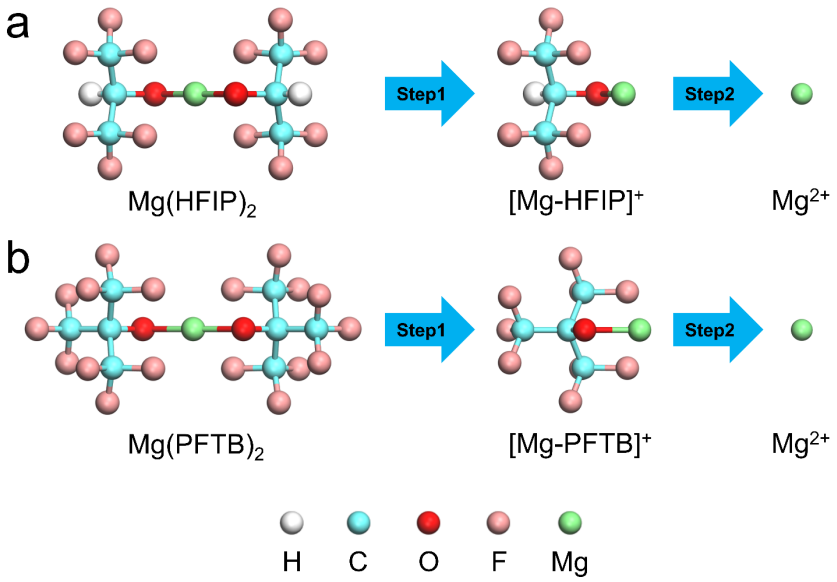

Figure S13. Desolvation process. The process of removing (a) $HFIP^-$ and (b) $PFTB^-$ from Mg^{2+} respectively.

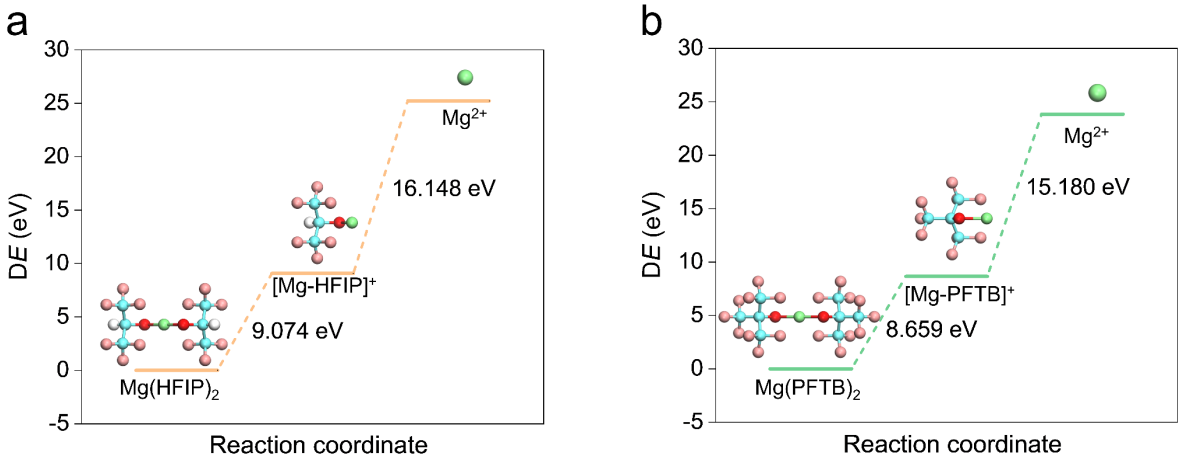

Figure S14. The desolvation steps for (a) $Mg(HFIP)_2$ and (b) $Mg(PFTB)_2$ electrolytes.

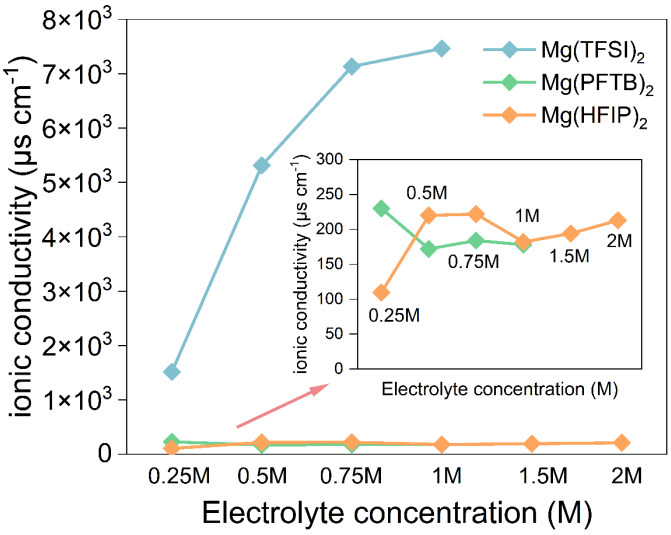

Figure S15. Ionic conductivity of different electrolytes at room temperature at different concentration. Ionic conductivity is determined by testing with a conductivity meter.

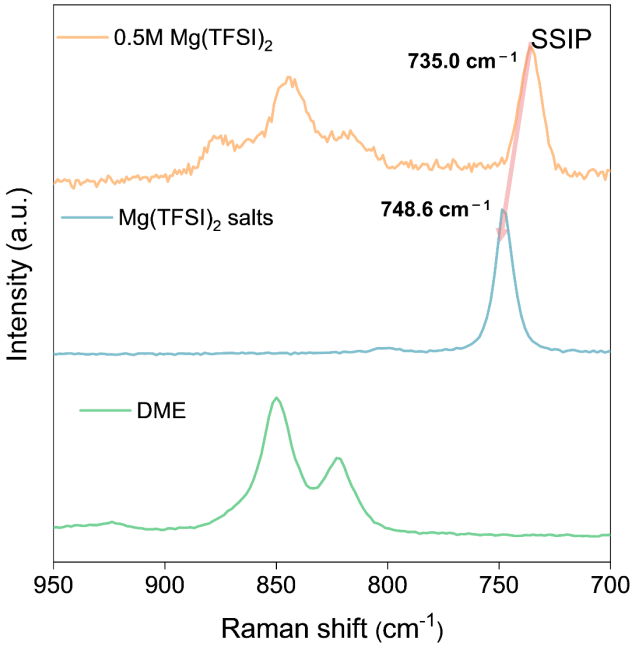

Figure S16. Raman spectra of pure DME, $Mg(TFSI)_2$ salts and 0.5 M $Mg(TFSI)_2$ electrolytes.

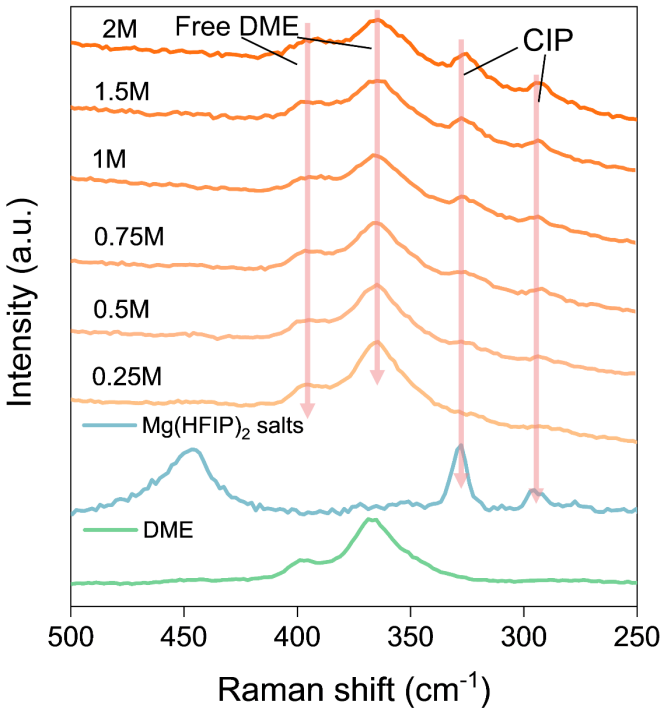

Figure S17. Raman spectra of pure DME, $Mg(HFIP)_2$ salts and $Mg(HFIP)_2$ electrolytes from 0.25 M to 2 M.

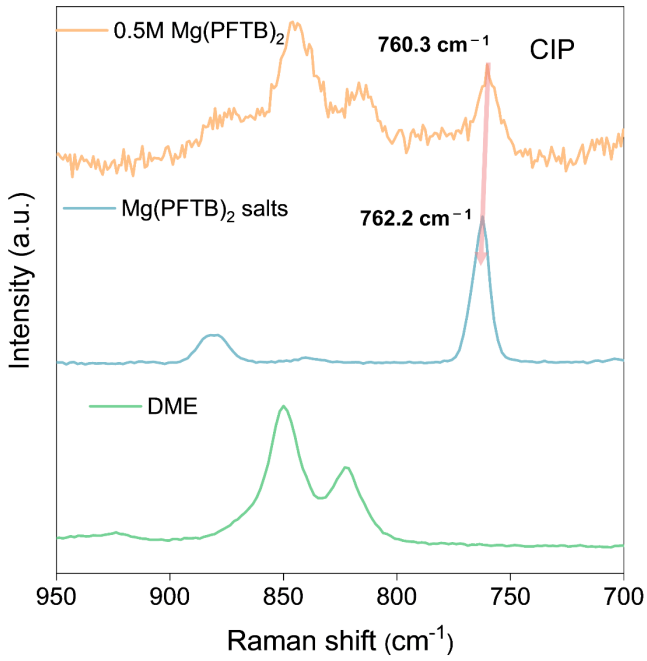

Figure S18. Raman spectra of pure DME, $Mg(PFTB)_2$ salts and 0.5 M $Mg(PFTB)_2$ electrolytes.

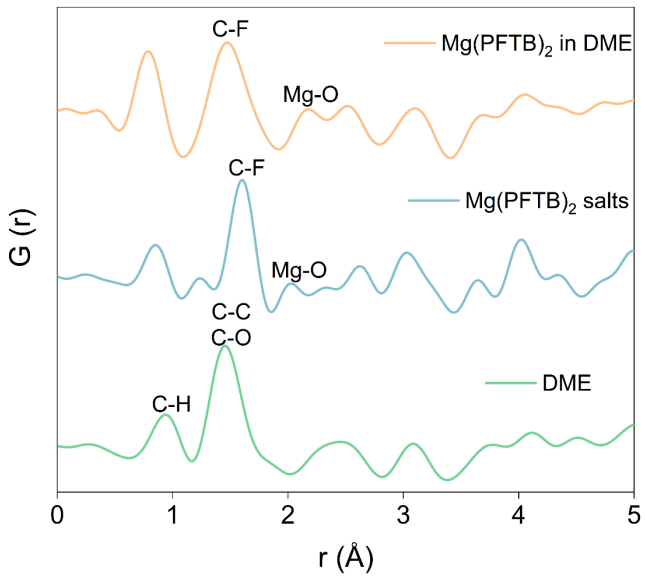

Figure S19. Pair distribution function of pure DME, $Mg(PFTB)_2$ salts and 0.5 M $Mg(PFTB)_2$ electrolyte.

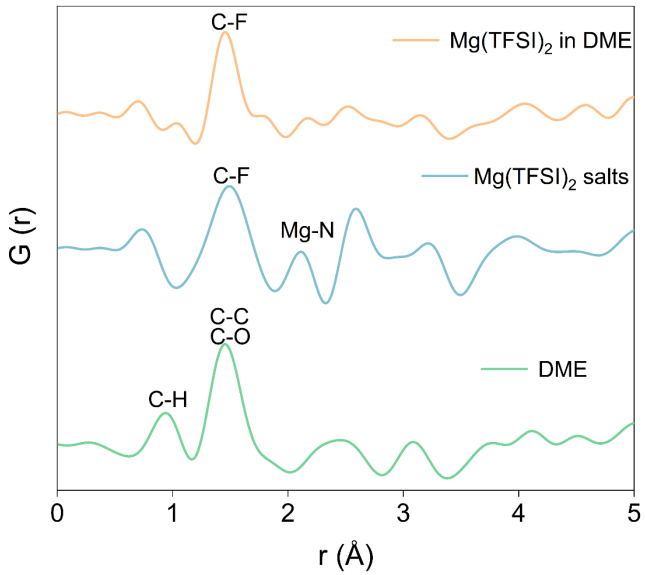

Figure S20. Pair distribution function of pure DME, $Mg(TFSI)_2$ salts and 0.5 M $Mg(TFSI)_2$ electrolyte.

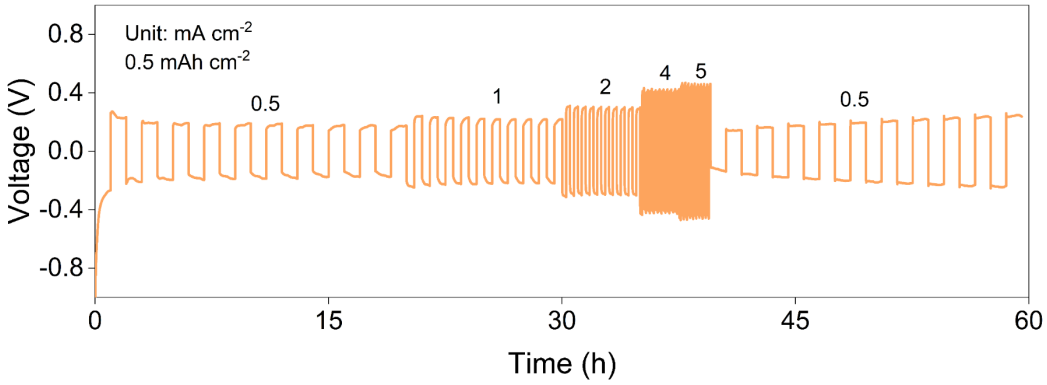

Figure S21. Overpotentials of Mg||Mg symmetric cells in 2 M $Mg(HFIP)_2$ electrolyte at various current densities from 0.5 to 5 mA cm^{-2} with a fixed capacity of 0.5 mAh cm^{-2}.

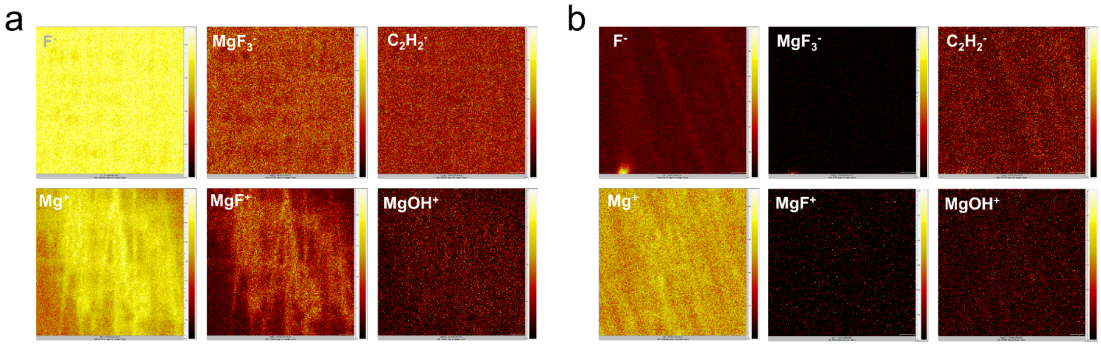

Figure S22. TOF-SIMS mapping images in negative mode of the SEI layers on the Mg metal anodes cycled in $Mg(TFSI)_2$ and $Mg(HFIP)_2$ electrolytes.

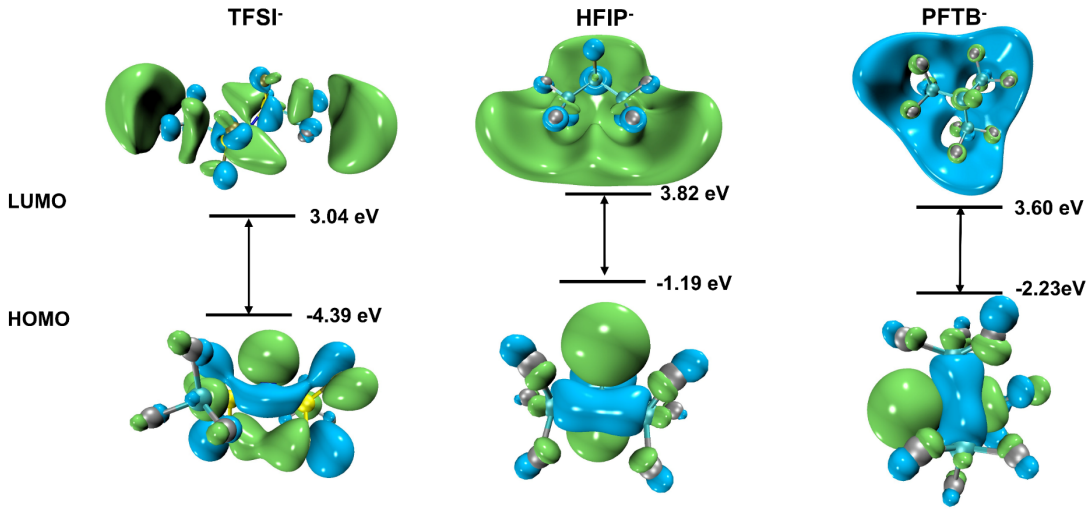

Figure S23. HOMO-LUMO energy level of [$TFSI^-$], [$HFIP^-$] and [$PFTB^-$] anions, the positive part of the LUMO and HOMO iso-surfaces are shown in light green and the negative part in light blue.

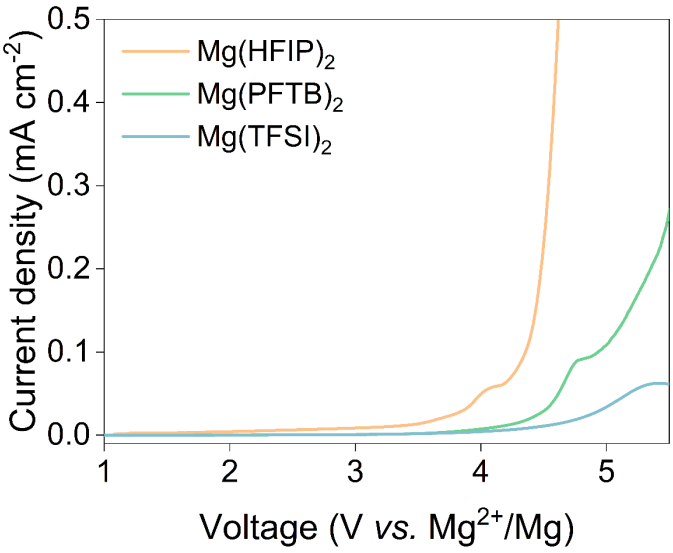

Figure S24. Oxidation stability of different electrolyte in Mo electrodes tested by linear sweep voltammetry.

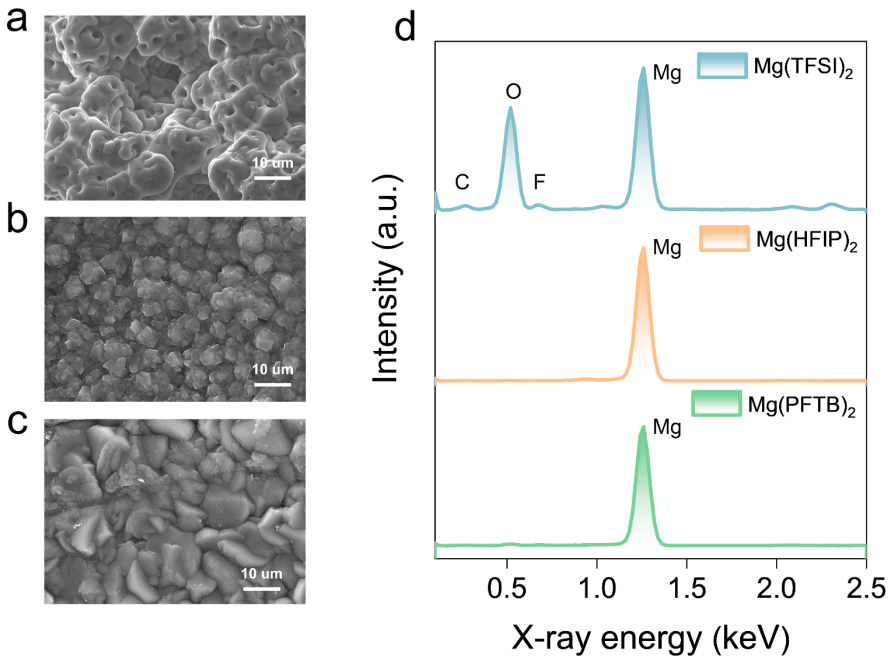

Figure S25. SEM images of deposited Mg on Cu electrodes at a current density of 0.1 mA cm^{-2} and 0.5 mAh cm^{-2} in (a) $Mg(TFSI)_2$, (b) $Mg(HFIP)_2$ and (c) $Mg(PFTB)_2$ electrolytes and (d) corresponding EDS maps.

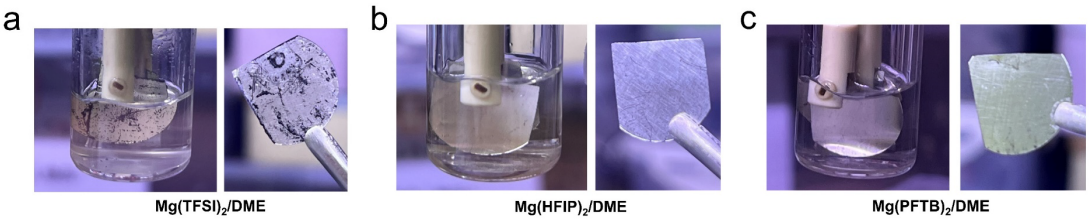

Figure S26. Optical photographs of Mg metal anode after cycled in different electrolytes.

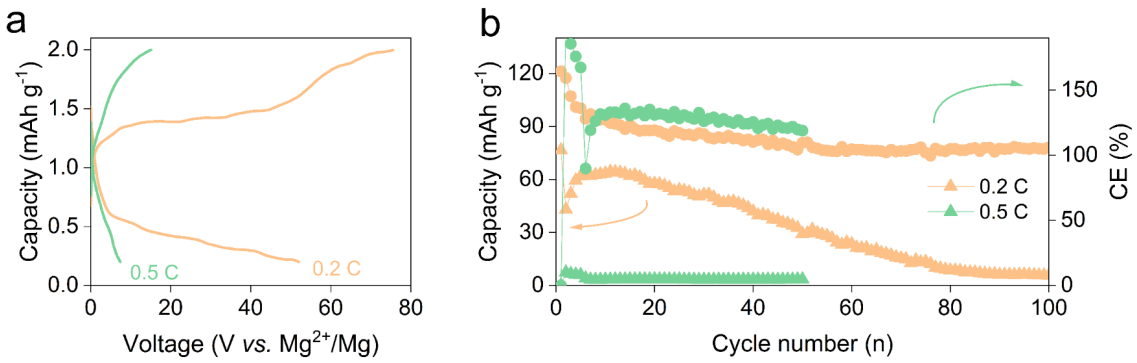

Figure S27. Mg||Mo_6S_8 full cell performance in $Mg(PFTB)_2$ electrolyte. (a) Charge/discharge profile with a voltage range of 0.2 − 2.0 V (vs. Mg^{2+}/Mg) and (b) corresponding cycling performance at 0.2 C and 0.5 C (1 C = 128.8 mAh g^{-1}).

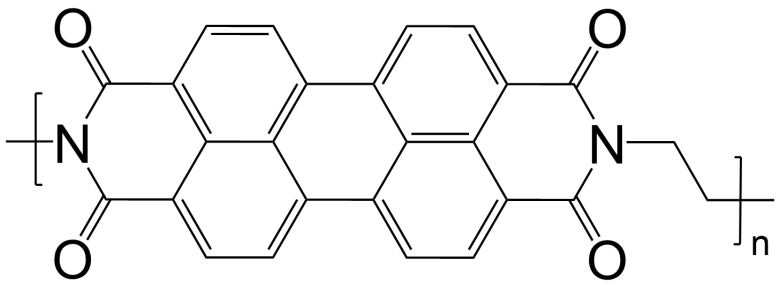

Figure S28. Detailed molecular structure of PDI-EDA materials.

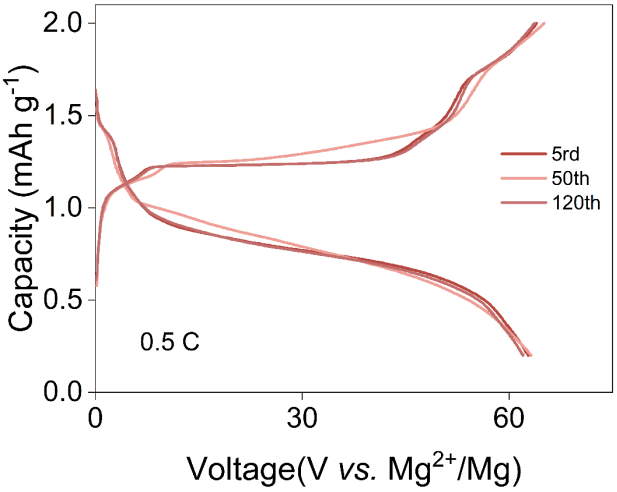

Figure S29. Selected charge/discharge curves with a voltage range of 0.2 − 2.0V (vs. Mg^{2+}/Mg) of Mg||Mo_6S_8 full cell in $Mg(HFIP)_2$ electrolyte.

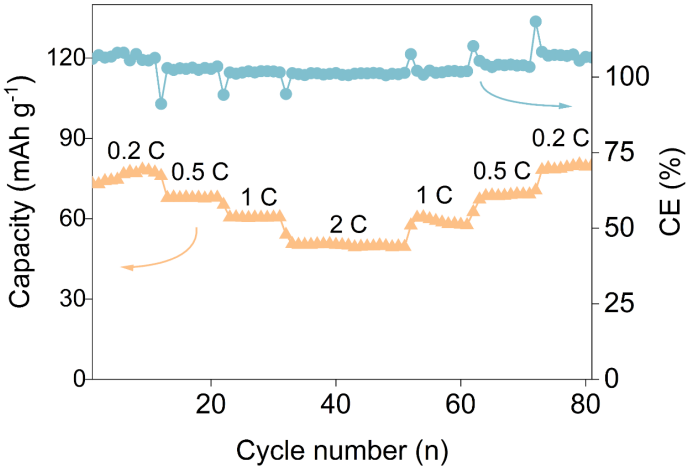

Figure S30. Mg||Mo_6S_8 full cell rate performance in $Mg(HFIP)_2$ electrolyte at various current densities from 0.2 to 2 C.

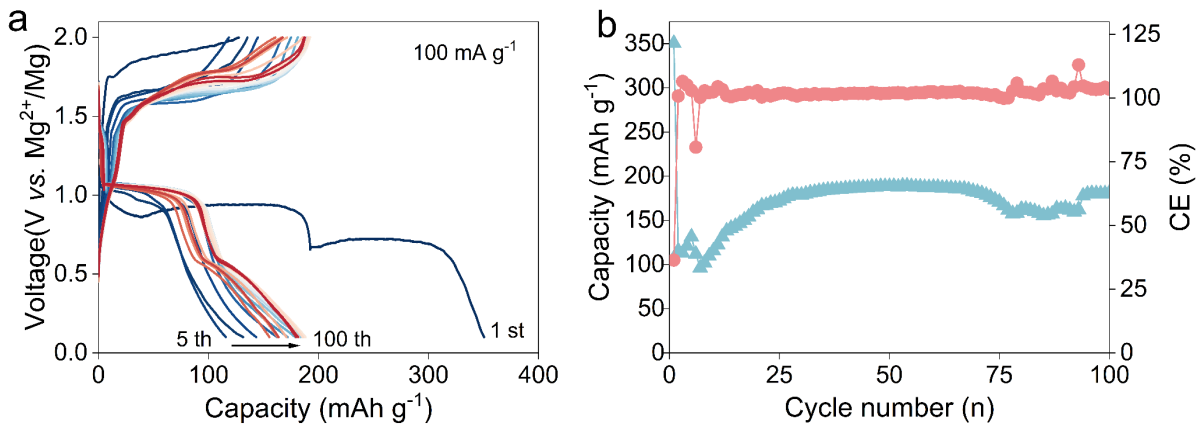

Figure S31. Mg||CuS full cell performance in $Mg(HFIP)_2$ electrolyte. (a) Charge/discharge profile with a voltage range of 0.1 − 2.0 V (vs. Mg^{2+}/Mg) and (b) corresponding cycling performance at 100 mAh g^{-1}.

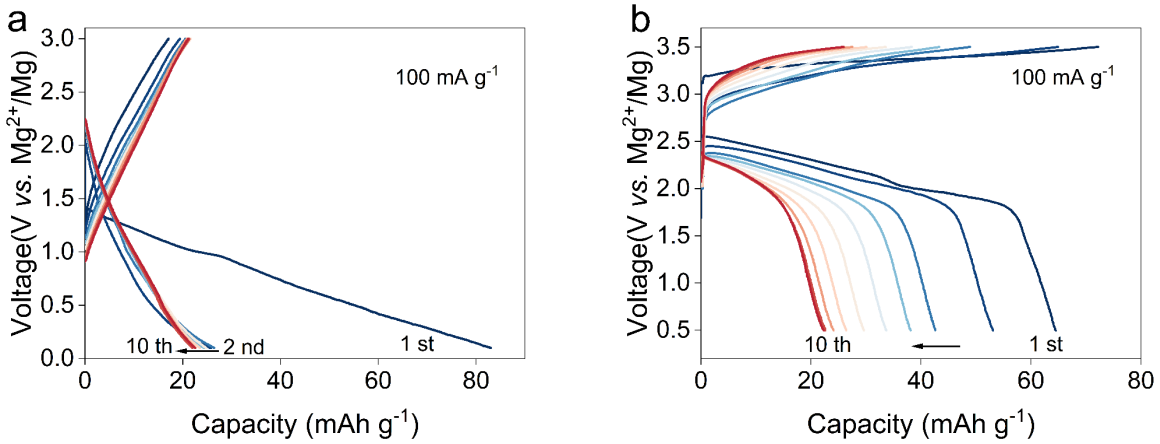

Figure S32. (a) Charge/discharge curves with a voltage range of 0.1 – 3.0 V (vs. Mg^{2+}/Mg) of Mg||MnO_2 full cell and (b) charge/discharge curves with a voltage range of 0.5 – 3.5 V (vs. Mg^{2+}/Mg) of Mg||FeHCF full cell in $Mg(HFIP)_2$ electrolyte.

Table S1. Crystal data and structure refinement for 2[Mg·2HFIP·DME]

Empirical formula	$C_{20}H_{24}O_8F_{24}Mg_2$
Formula weight	897
Temperature/K	296.15
Crystal system	triclinic
Space group	P-1
a/Å	10.513(5)
b/Å	10.598(5)
c/Å	16.827(9)
α/°	100.041(8)
β/°	102.944(9)
γ/°	110.107(8)
Volume/Å^3	1649.9(15)
Z	23
ρ_{calc}g/cm^3	1.674
μ/mm^{-1}	0.364
F (000)	808.0
Crystal size/mm^3	2 × 2 × 2
Radiation	Mo Kα (λ = 0.71073)
2θ range for data collection/°	2.582 to 55.898
Index ranges	-13 ≤ h ≤ 11, -13 ≤ k ≤ 13, -22 ≤ l ≤ 22
Reflections collected	11145
Independent reflections	7675 [R_{int} = 0.1002, R_{sigma} = 0.0909]
Data/restraints/parameters	7675/0/491
Goodness-of-fit on F^2	1.771
Final R indexes [I>=2σ (I)]	R_1 = 0.1507, wR_2 = 0.4529
Final R indexes [all data]	R_1 = 0.2008, wR_2 = 0.4907
Largest diff. peak/hole / e Å^{-3}	0.93/-0.93

The CIF files have been deposited in the **Cambridge Crystallographic Data Centre (CCDC)** with deposition numbers 2245741.

Table S2. Performance comparison of Mg metal batteries that store Mg^{2+} ions in simple Mg-salt electrolytes

Electrolyte	Cathode	Cycle number (n)	Voltage (V)	Capacity (mAh g^{-1})	Specific energy (Wh kg^{-1})	Ref.
$Mg[B(hfip)_4]_2$/DME	Mo_6S_8	200	~1.1	~75	82.5	7
$Mg[B(hfip)_4]_2$/DME	PANI	100	~1.4	~160	224	7
$Mg(OTf)_2$ + CP	PTCDA	120	~1.5	~70	105	8
$Mg[B(hfip)_4]_2$/DME	MoS_2	100	~0.67	~120	80	9
$Mg(TFSI)_2$/DME+S2	Mo_6S_8	100	~0.9	~80	72	10
$Mg(OTf)_2$+MOEA	Mo_6S_8	300	~0.9	~60	54	11
$Mg[B(Otfe)_4]_2$/THF	Mo_6S_8	210	~0.75	~60	45	12
$Mg[Al(hfip)_4]_2$/DME	Mo_6S_8	50	~0.8	~50	40	13
$Mg(HFIP)_2$/DME This work	**PDI-EDA**	**400**	**~1.4**	**~145**	**203**	**/**

References

(1) Ren, W.; Xiong, F.; Fan, Y.; Xiong, Y.; Jian, Z. Hierarchical Copper Sulfide Porous Nanocages for Rechargeable Multivalent-Ion Batteries. *ACS Appl. Mater. Interfaces* **2020**, *12* (9), 10471-10478.

(2) Zuo, C.; Xiong, F.; Wang, J.; An, Y.; Zhang, L.; An, Q. MnO2 Polymorphs as Cathode Materials for Rechargeable Ca-Ion Batteries. *Adv. Funct. Mater.* **2022**, *32* (33), 2202975.

(3) Huang, G.; Lao, Z.; He, Z.; Xiong, F.; Tan, S.; Huang, M.; Thompson, G.; An, Q.; Mai, L. Mg-substituted Prussian blue as a low-strain cathode material for aqueous Fe-ion batteries. *Chem. Commun.* **2023**, *59* (27), 4067-4070.

(4) Chen, Y.; Jaegers, N. R.; Wang, H.; Han, K. S.; Hu, J. Z.; Mueller, K. T.; Murugesan, V. Role of Solvent Rearrangement on Mg(2+) Solvation Structures in Dimethoxyethane Solutions using Multimodal NMR Analysis. *J. Phys. Chem. Lett.* **2020**, *11* (15), 6443-6449.

(5) Adams, B. D.; Zheng, J.; Ren, X.; Xu, W.; Zhang, J. G. Accurate Determination of Coulombic Efficiency for Lithium Metal Anodes and Lithium Metal Batteries. *Adv. Energy Mater.* **2017**, *8* (7), 1702097.

(6) de la Cruz, C.; Molina, A.; Patil, N.; Ventosa, E.; Marcilla, R.; Mavrandonakis, A. New insights into phenazine-based organic redox flow batteries by using high-throughput DFT modelling. *Sustain. Energy Fuels* **2020**, *4* (11), 5513-5521.

(7) Li, C.; Shyamsunder, A.; Key, B.; Yu, Z.; Nazar, L. F. Stabilizing magnesium plating by a low-cost inorganic surface membrane for high-voltage and high-power Mg batteries. *Joule* **2023**, *7*, 1-16.

(8) Yang, G.; Li, Y.; Wang, J.; Lum, Y.; Lim, C. Y. J.; Ng, M.-F.; Zhang, C.; Chang, Z.; Zhang,

Z.; Handoko, A. D.; et al. Realizing horizontal magnesium platelet deposition and suppressed surface passivation for high-performance magnesium metal batteries. *Energy Environ. Sci.* **2024**, *17*, 1141-1152.
(9) Li, Z.; Mu, X.; Zhao-Karger, Z.; Diemant, T.; Behm, R. J.; Kubel, C.; Fichtner, M. Fast kinetics of multivalent intercalation chemistry enabled by solvated magnesium-ions into self-established metallic layered materials. *Nat. Commun.* **2018**, *9* (1), 5115.
(10) Wang, F.; Hua, H.; Wu, D.; Li, J.; Xu, Y.; Nie, X.; Zhuang, Y.; Zeng, J.; Zhao, J. Solvent Molecule Design Enables Excellent Charge Transfer Kinetics for a Magnesium Metal Anode. *ACS Energy Lett.* **2023**, *8* (1), 780-789.
(11) Du, Y.; Chen, Y.; Tan, S.; Chen, J.; Huang, X.; Cui, L.; Long, J.; Wang, Z.; Yao, X.; Shang, B.; et al. Strong solvent coordination effect inducing gradient solid-electrolyte-interphase formation for highly efficient Mg plating/stripping. *Energy Storage Mater.* **2023**, *62*, 102939.
(12) Ren, W.; Wu, D.; NuLi, Y.; Zhang, D.; Yang, Y.; Wang, Y.; Yang, J.; Wang, J. An Efficient Bulky Mg[B(Otfe)4]2 Electrolyte and Its Derivatively General Design Strategy for Rechargeable Magnesium Batteries. *ACS Energy Lett.* **2021**, *6* (9), 3212-3220.
(13) Herb, J. T.; Nist-Lund, C. A.; Arnold, C. B. A Fluorinated Alkoxyaluminate Electrolyte for Magnesium-Ion Batteries. *ACS Energy Lett.* **2016**, *1* (6), 1227-1232.